ARL-TR-8975 ● JUNE 2020

DEVCOM ARMY RESEARCH LABORATORY

Advanced X-ray Computed Tomography of Voids and Porosity in As-Cast FeMnAl Steel Alloy Material

by William H Green, Bryan A Cheeseman, Daniel M Field, and Krista R Limmer

NOTICES

Disclaimers

The findings in this report are not to be construed as an official Department of the Army position unless so designated by other authorized documents.

Citation of manufacturer's or trade names does not constitute an official endorsement or approval of the use thereof.

Destroy this report when it is no longer needed. Do not return it to the originator.

ARL-TR-8975 ● JUNE 2020

Advanced X-ray Computed Tomography of Voids and Porosity in As-Cast FeMnAl Steel Alloy Material

William H Green, Bryan A Cheeseman, Daniel M Field, and Krista R Limmer
Weapons and Materials Research Directorate, CCDC Army Research Laboratory

REPORT DOCUMENTATION PAGE

Form Approved
OMB No. 0704-0188

1. REPORT DATE *(DD-MM-YYYY)*	2. REPORT TYPE	3. DATES COVERED (From - To)
June 2020	Technical Report	1 August 2018–31 January 2020

4. TITLE AND SUBTITLE
Advanced X-ray Computed Tomography of Voids and Porosity in As-Cast FeMnAl Steel Alloy Material

5a. CONTRACT NUMBER

5b. GRANT NUMBER

5c. PROGRAM ELEMENT NUMBER

6. AUTHOR(S)
William H Green, Bryan A Cheeseman, Daniel M Field, and Krista R Limmer

5d. PROJECT NUMBER

5e. TASK NUMBER

5f. WORK UNIT NUMBER

7. PERFORMING ORGANIZATION NAME(S) AND ADDRESS(ES)
CCDC Army Research Laboratory
ATTN: FCDD-RLW-MB
Aberdeen Proving Ground, MD 21005

8. PERFORMING ORGANIZATION REPORT NUMBER
ARL-TR-8975

9. SPONSORING/MONITORING AGENCY NAME(S) AND ADDRESS(ES)

10. SPONSOR/MONITOR'S ACRONYM(S)

11. SPONSOR/MONITOR'S REPORT NUMBER(S)

12. DISTRIBUTION/AVAILABILITY STATEMENT
Approved for public release; distribution is unlimited.

13. SUPPLEMENTARY NOTES
ORCID ID(s): Limmer, 0000-0003-4775-5876

14. ABSTRACT

The X-ray computed tomography (XCT) technique is a widely applicable and powerful nondestructive inspection modality to evaluate and analyze geometrical and physical characteristics of materials, especially internal structures and features. XCT is applicable to metals, ceramics, plastics, and polymer and mixed composites, as well as components and materiel. The US Army Combat Capabilities Development Command (CCDC) Army Research Laboratory (ARL) and its partners are currently investigating the use of cast iron-manganese-aluminum (FeMnAl) steel alloy material in support of weight reduction initiatives in Army development programs. Steel alloy FeMnAl has been identified as a key enabling material technology to reduce the weight in ground combat vehicle systems. A set of FeMnAl blocks, each approximately 50.8 mm (2 inches) thick by 76.2 mm (3 inches) wide by 76.2 mm (3 inches) long, which had been sectioned from an industrially cast ingot (~12,000 lb), were individually scanned by XCT using a conventional 450-kV X-ray source and a solid-state flat panel detector. Due mainly to the thickness of the blocks, as well as a desire to keep geometric unsharpness relatively small, which affected overall scan geometry (setup), the scans had a very low response at the detector through the FeMnAl blocks. With the calibrated detector response through air (i.e., around a block) at 85%–90%, the response through the block was only 5%–10%. This report covers the XCT scanning parameters and overall protocol used to mitigate the very low intensity throughput and achieve acceptable scan image results; the overall quality of the FeMnAl blocks and the image processing methods used to segment porosity and void features in the blocks; and quantitative results of porosity and void content, number of overall pores/voids, and pore/void volume distribution.

15. SUBJECT TERMS
porosity/voids, FeMnAl, X-ray computed tomography, image processing, quantitative

16. SECURITY CLASSIFICATION OF:			17. LIMITATION OF ABSTRACT	18. NUMBER OF PAGES	19a. NAME OF RESPONSIBLE PERSON
a. REPORT	b. ABSTRACT	c. THIS PAGE			William H Green
Unclassified	Unclassified	Unclassified	UU	25	19b. TELEPHONE NUMBER (Include area code) (410) 306-0817

Contents

List of Figures

List of Tables

1. Introduction and Background

The X-ray computed tomography (XCT) technique is a widely applicable and powerful nondestructive inspection modality to evaluate and analyze geometrical and physical characteristics of materials, especially internal structures and features. XCT is applicable to metals, ceramics, plastics, and polymer and mixed composites, as well as components, assemblies, and materiel. The principal advantage of XCT is that it provides densitometric (that is, radiological density and geometry) images of thin cross sections through an object in a noninvasive manner. Because of the absence of structural superimposition, images are much easier to interpret than conventional radiological images.[1–4]

The US Army Combat Capabilities Development Command (CCDC) Army Research Laboratory (ARL) and its partners are currently investigating the use of cast iron-manganese-aluminum (FeMnAl) steel alloy material in support of weight reduction initiatives in Army development programs. Steel alloy FeMnAl has been identified as a key enabling material technology to reduce the weight in ground combat vehicle systems. A large industrial FeMnAl alloy ingot several meters (feet) long, 1.32 m (52 inches) wide, and 0.305 m (12 inches) thick with a nominal chemistry of Fe-30Mn-9Al-0.8Si-1C-0.5Mo was produced by electric arc furnace melting in a 40T heat and subsequent casting using a bottom pour method, after which a normalization heat treatment was performed. XCT scanning of several specimens sectioned from three different solidification areas of the ingot determined the internal mesoscale structure of these areas and identified a number of significant individual features. The solidification areas included a central region in the middle (thickness) of the ingot and regions just inside the outside edges of the ingot along the 1.32-m width. In this report the locations and organization of the sectioned specimens will be given. The XCT scanning parameters and overall protocol used to mitigate the very low intensity throughput and achieve acceptable scan image results will be discussed, as well as scan results of interior structure and features of each solidification area. Image processing methods used to segment porosity features in the FeMnAl blocks will also be discussed.

2. Preparation of FeMnAl Specimens

After the normalization treatment, a 76.2-mm (3-inch)-wide slice from just below the hot top of the ingot was removed for analysis. A water jet method was used to remove fourteen 50.8- × 76.2- × 76.2-mm (2- × 3- × 3-inch) blocks from the ingot slice according to the schematic in Fig. 1, in which the width of the ingot is left-to-right, the thickness direction is vertical, and the 76.2-mm (3-inch) slice direction is

into the page. The solidification direction is from the outside toward the inside, and the filling or casting direction is coming out of the page. Six blocks were sectioned from the middle interior of the ingot slice, labeled C1 to C6, as shown in Fig. 1. Four blocks each were sectioned from two outside regions on either side of the middle interior region to be representative of possible solidification effects in the same area, labeled A1 to A4 and B1 to B4, as shown in Fig. 1.

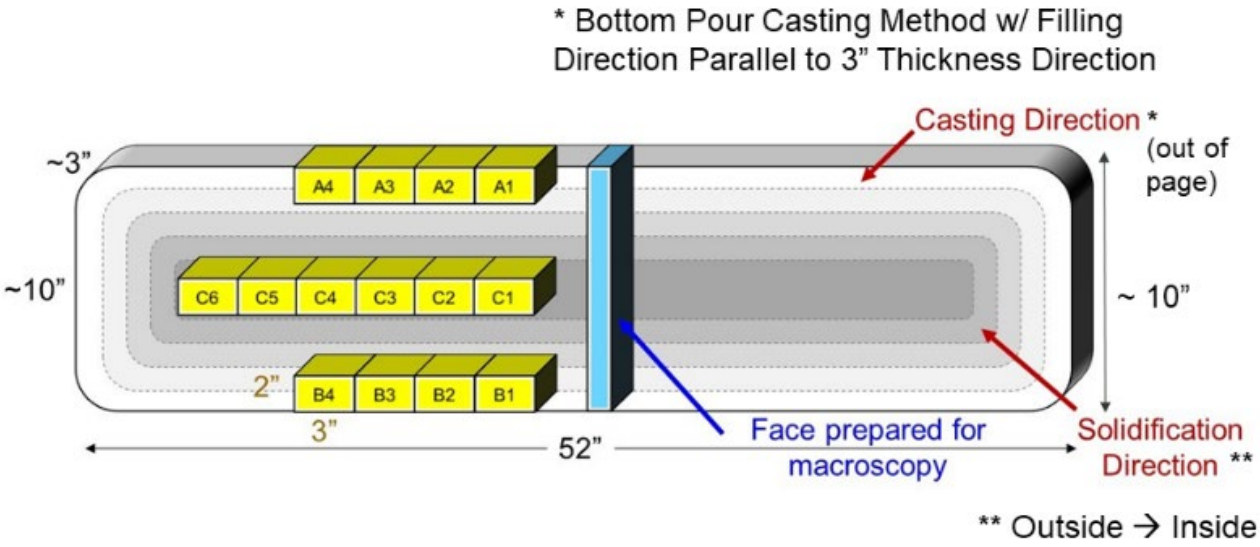

Fig. 1 Schematic of specimen blocks sectioning

3. XCT Scanning Procedures

Given that the approximately 76.2- × 76.2-mm (3- × 3-inch) steel alloy FeMnAl blocks were 50.8 mm (2 inches) thick, the attenuation of 450-keV maximum energy polychromatic Bremsstrahlung X-rays was high. Although not generally explicitly stated in standards on XCT practice,[1,5] a general rule of thumb sometimes used in industrial XCT is to set up the scan procedure such that approximately 50% of the initial X-ray intensity from the X-ray source is attenuated by the object of interest. The purpose of this approach is to have a balance between image contrast and intensity, or signal, at the detector, and hence signal-to-noise ratio (S/N), in the XCT scans. XCT scans can still be performed with attenuation factors significantly below or above 50% with resultant effects of loss of contrast or loss of detector signal and possibly decrease in S/N. However, XCT images generated from these types of scans can still show pertinent physical information and features and provide acceptable physical data about a specimen.

Figure 2 shows a 2-D X-ray projection image through the 50.8-mm (2-inch) thickness of one of the FeMnAl blocks using the X-ray technique (tube energy and current) of the XCT scan method, the parameters of which are given in Table 1.

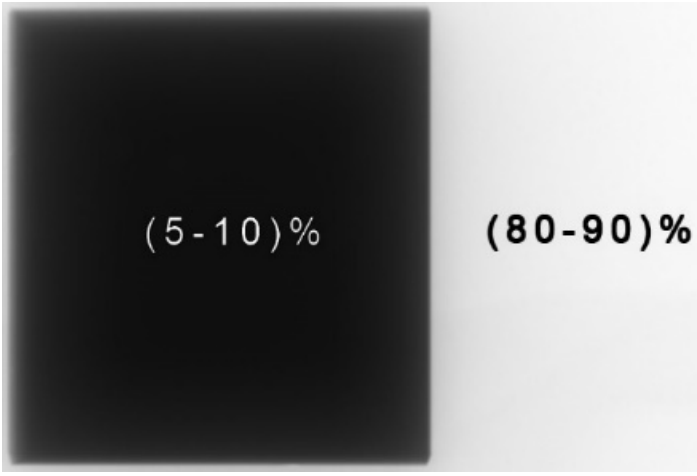

Fig. 2 Offset and gain corrected projection image through FeMnAl block (dark)

Table 1 XCT scanning parameters

X-ray voltage (peak)	450 kV
X-ray energy (peak)	450 keV
X-ray current	1550 µA
Detector sample rate	1 frame/s (fps)
X-ray focal spot size	400 µm
Source-to-image distance	875 mm
Source-to-object distance	575 mm
Magnification	1.52
Detector element pitch	200 µm
Effective pixel pitch	131 µm
Unsharpness	1.04 pixels
Frame average	4
No. of projections (views)	2200
Source filter (Cu)	15.9 mm (0.625 inch)

The detector field of view around the relatively dark block is unsaturated and has an intensity level of about 85% of maximum, or saturation level. The intensity level through the thickness of the block is only about 6%, well below the general 50% transmission rule of thumb. It is extremely difficult to distinguish any individual features or significant density variations in the single projection image, which has been frame averaged. The XCT scan method used four times (4×) frame averaging and projection image "oversampling" to maximize the detection of density variations within the FeMnAl blocks. When an image with random noise is frame averaged an *n* number of times, the magnitude of the noise fluctuation is decreased by the factor of the square root of *n*. In other words, the percent of original random noise remaining after *n* frames is averaged is $100 * (\frac{1}{\sqrt{n}})$.[6] It is evident from the functionality of this equation that as the number of frames increases, the improvement in noise reduction becomes less and less effective. Thus, although

frame averaging does not add a large amount of processing time when applied to a few images, such as a few digital radiographs, there is a tradeoff between improvement of images and processing time spent if a relatively large number of images will be averaged, such as is the case in extensive and/or oversampled XCT scans.

A commonly used number of frames averaged is four, which reduces noise fluctuation by 50%, because it significantly reduces the noise level in a reasonable amount of processing time for large data sets. In Nyquist–Shannon sampling theory,[7] given a polychromatic (i.e., multiple frequency) temporal (or spatial) continuous function, f(x), with known maximum spatial frequency X_{max}, it is completely determined by giving its sampled ordinates at a series of points spaced less than or equal to a distance of $1/(2X_{max})$ apart. The threshold $2X_{max}$ is called the Nyquist rate and is an attribute of the continuous spatial input f(x) being sampled. The sample rate, R, must exceed the Nyquist rate for the samples to suffice to represent f(x). The threshold R/2 is called the Nyquist frequency and is an attribute of the sampling equipment. The number of projections used to reconstruct an XCT data set is one of the determining factors in image quality. Too large an interval between projections, or undersampling, results in the loss of accurate information about the physical geometry of the scanned object. Reconstructed images of undersampled FeMnAl blocks would likely exhibit some type of regular angular variation in gray levels and associated loss of internal and edge physical information. Oversampling the scan space provides finer physical geometric information for the reconstruction process and helps to mitigate the effects of very high X-ray attenuation and related noise in the resultant XCT data. The scans of the blocks purposely collected twice as many projections as normal, which is based on 1.5 times the pixel width of the specimen field of view, to oversample the scan space during the 360° rotation. Application of effective frame averaging and oversampling the scan space are illustrative of the principle of obtaining the best quality XCT data set given the material of interest and overall scan considerations.

4. Qualitative and Quantitative XCT Results

4.1 Qualitative Image Results

Figure 3 shows images of blocks A2 and A4 (left to right), B2, B2 again, and B3 (left to right), and C3, C2, and C4 (left to right) in the top (a), middle (b), and bottom (c) rows, respectively, in which the spatial views are in the 50.8-mm (2-inch)-thickness direction (front views), except for the second B2 image, which is a side view. Block A2 has one small porosity indication circled in black while block A4 has a significantly larger void feature about 3.1 mm (0.12 inch) in

diameter, which is atypical of the A blocks scanned, including A2, A3, and A4. Block A1 was not available for scanning. In general, the A blocks have a higher-quality level as determined by the number and sizes of detected discontinuities or features than both the B and C blocks. In fact, block A3 does not have any discernible discontinuities. The images of blocks B2 and B3 show features within multiple blocks in this set (B1–B4), all of which were scanned, including small voids, relatively short cracks starting at edges or corners, and missing material at edges or corners. Blocks B1, B2, and B4 all have porosity, with B1 and B2 having a single small pore and B4 having multiple small pores. Blocks B2, B3, and B4 all have short cracks starting at edges or corners, with B2 having roughly the longest crack. Blocks B1, B2, and B3 all have significant amounts of missing material along an edge or in a corner, with B1 having a relatively wide section of missing material about 38 mm (1.5 inch) long along an edge into an upper corner. Thus, overall the B blocks have more discontinuities or features than the A blocks. It is reasonable to consider the missing material of the B blocks to be qualitatively like large voids, since if nominal material was in close proximity to the sectioning locations, it would have remained with the blocks. In contrast, the images of blocks C3, C2, and C4 have a very large oval void feature approximately 6.8 mm (0.27 inch) × 8.1 mm (0.32 inch) on the left side, a large void feature intersecting with the right vertical edge, and a large void feature about 6.5 mm (0.26 inch) in diameter on the right side, respectively, which is approximately in the middle of the 50.8-mm (2-inch) thickness. Relatively large internal voids as well as some voids intersecting edges or corners are typical of the C blocks, five of which (C2–C6) were scanned in their as-cast state since block C1 had already been mechanically rolled.

a. Internal front view images of blocks A2 (left) and A4 (right) showing very small void (circled) and larger void in A2 and A4, respectively

b. Internal front and side view images of block B2 and internal front view image of block B3 (right) showing small void (circled) and crack (boxed) in B2 and missing material in B3

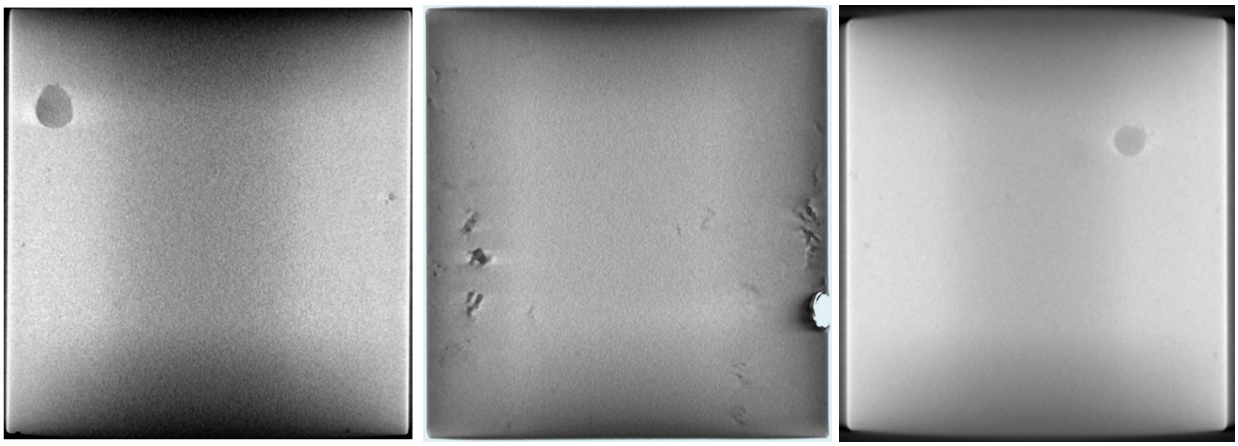

c. Internal front view images of blocks C3, C2, and C4 from left to right showing very large void, intersecting edge void, and large void in C3, C2, and C4, respectively

Fig. 3 Set of representative internal front and side view images of several blocks, including (a) blocks A2 and A4, (b) blocks B2 and B3, and (c) blocks C3, C2, and C4

Figure 4a shows images of block C4, with the image on the left relatively close to an outer face and the other images clearly showing not one, but two, large void features at approximately the middle thickness of the block. The nature of the porosity and voids in block C4, which were representative of all of the C blocks, clearly changed from extended and asymmetric, or more crack-like, features nearer to the outside of the block to significantly more symmetric, rounded voids in the center region of the block, the edge or corner voids notwithstanding. The A and B blocks do not have similar asymmetric crack-like features, and their porosity or voids are generally significantly smaller. Therefore, the overall quality of the C blocks is the worst of the three sets. Figure 4b shows one of the large voids in a sectioned side view, the same void in a rotated and sectioned (in two directions)

view, and both voids in a similarly rotated and sectioned view on the left, middle, and right, respectively. It is readily apparent from the images in Figs. 3 and 4 that the gray levels are not uniform across the specimens and generally vary from one local area to another, which was essentially due to the very high X-ray attenuation by the FeMnAl steel and resulting beam hardening. Thus, a simple global gray level threshold was insufficient to segment porosity and void features from nominal material.

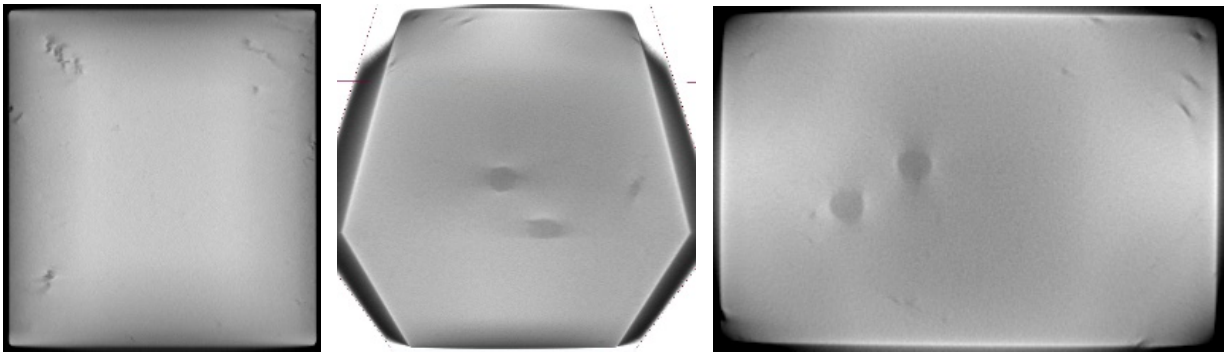

a. Internal images of block C4 showing dendritic porosity (left) and voids (center and right)

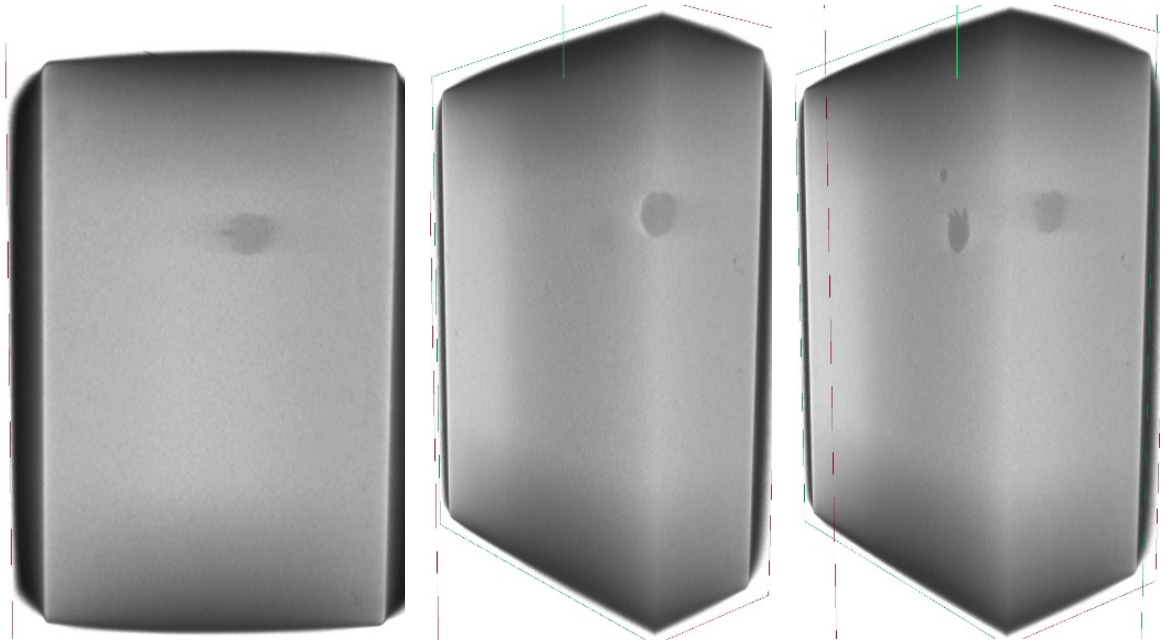

b. Sectioned side view image (left) and rotated and sectioned view images of block C4

Fig. 4 (a) Internal images of block C4 showing dendritic porosity and voids, and (b) other sectioned and rotated/sectioned internal images of block C4

4.2 Image Processing Methodology

A stack of approximately 50.8-mm (2-inch) × 76.2-mm (3-inch) cross-sectional images of block C4 was exported from the reconstructed XCT data. A series of image processing steps was applied to each image in the stack to segment, or binarize, porosity and void features from nominal material, including nonlocal means (NLM) filtering for noise reduction, adaptive mean-based thresholding, dilation, despeckling, and location-dependent selective masking. Unlike "local mean" filters, which take the *mean* value of a group of pixels surrounding a target pixel to smooth the image, NLM filtering takes a mean of all pixels in the image, weighted by how similar these pixels are to the target pixel. This results in much greater post-filtering clarity and less loss of detail in the image compared with local mean algorithms.[8] If compared with other well-known denoising techniques, NLM adds "method noise" (i.e., error in the denoising process), which looks more like *white noise*, which is desirable because it is typically less disturbing in the denoised product.[9]

Figure 5 shows an image from the stack, the NLM filtered (three times) image, and the image after standard global thresholding on the left, middle, and right, respectively. Standard global thresholding, which segments an entire image based on a constant gray level, does not segment any porosity or voids from nominal material. In adaptive thresholding the segmentation threshold of a pixel/voxel is a function of the gray levels of all the pixels/voxels around it within a selected radius.[10] Adaptive thresholding can segment local gray level variations, indicating discontinuities when they are present over relatively global (i.e., low spatial frequency) gray scale changes, such as is the case in this low throughput, beam-hardened, nonuniform image stack. In this work mean-based thresholding, in which the segmentation threshold is based on the mean gray levels of surrounding pixels, was used. This was performed using both a lower and upper threshold, below which all pixels were segmented to black and above which all pixels were segmented to white (i.e., nominal material), respectively, while the adaptive segmentation was applied in between the thresholds. Dilation and despeckling processes were performed on segmented binary (binarized) images. Dilation is used to "grow" nominal material, and despeckling is generally used to remove black or white "speckles" considered to be due to noise levels or artifacts.[10] In this work dilation was used to generate more representative binarized images based on comparison of sizable features in unbinarized data and prepare the images for minimal despeckling to eliminate small black speckles, but not discernible porosity or voids. In more ideal cases of closer to optimal X-ray throughput data sets with low noise levels, high feature contrast, and minimal or no beam hardening or artifacts, these steps may not be necessary to successfully segment images.

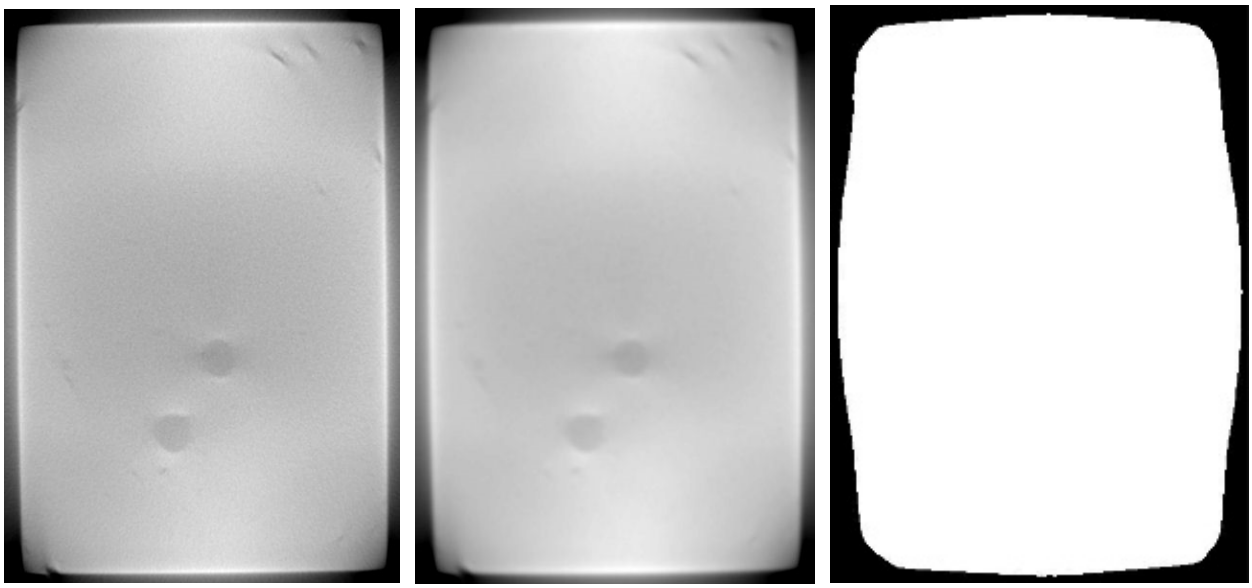

Fig. 5 Image processing of stack slice in block C4 using global thresholding on right

Lastly, selective masking was used to eliminate black banding, which was present in the binarized images close to the outside surfaces of the block, but not in the corner regions. These relatively long, linear expanses of black pixels occurred due to edge attenuation effects from beam hardening. Since these features are related to the block geometry and always occurred in the same regions with the same orientations, a location-dependent mask was created to turn all the black pixels in the mask region to white.[11] Figure 6a shows the same image as in Fig. 5 (without global thresholding) after both 3xNLM filtering and adaptive mean-based thresholding (left), dilation, despeckling, and selective masking from left to right. This series of image processing steps resulted in a fairly good segmented representation of porosity and void content in the material. Figure 6b shows a second example of the image processing steps applied to another image at a different location in the stack, in which 3xNLM filtering (left), adaptive mean-based thresholding, dilation and despeckling, and selective masking were applied from left to right.

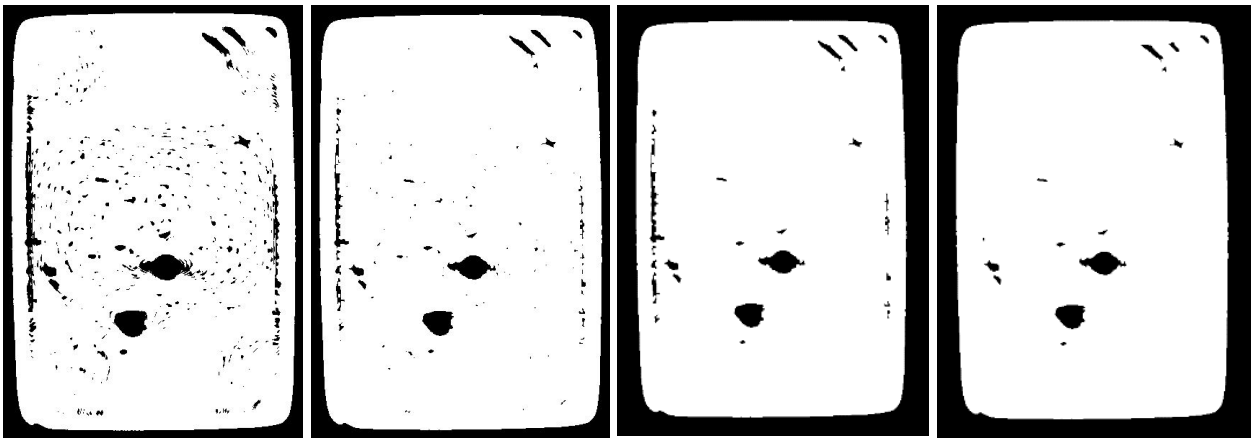

a. 3xNLM filtering and adaptive mean-based thresholding (left), dilation, despeckling, and selective masking image processing steps from left to right

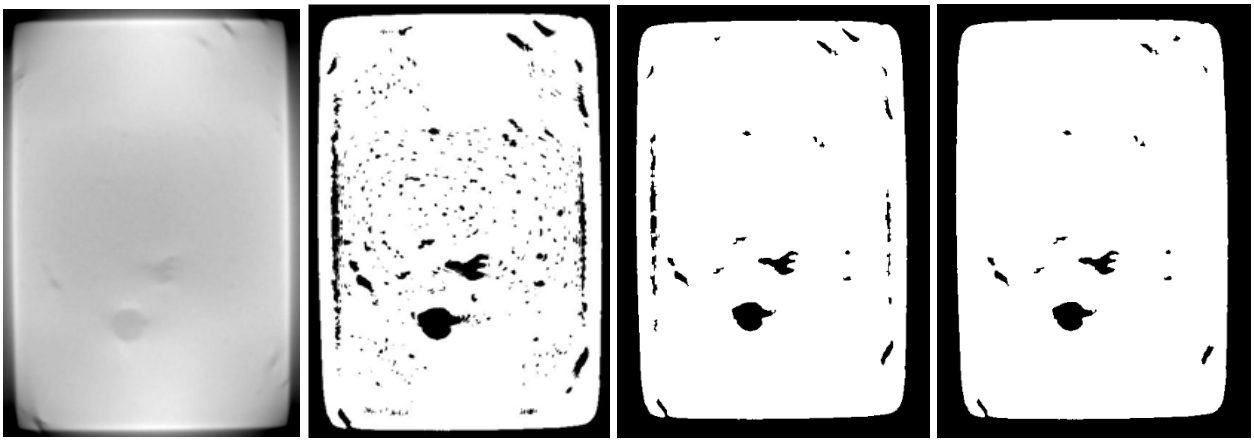

b. 3xNLM filtering (left), adaptive mean-based thresholding, dilation and despeckling, and selective masking image processing steps from left to right

Fig. 6 (a) Example of multistep image processing method applied to slice image in block C4 image stack, and (b) multistep image processing method applied to different slice image in stack

4.3 Quantitative Porosity and Void Results

The segmented image stack of the block volume provides the necessary binary data to analyze the spatial distribution and size composition of the porosity/void content, since each image represents a one-voxel-thick slice. Two- and three-dimensional analysis tools were used in CT-Analyser (Bruker Corporation) to inspect the binary stack and determine the porosity and void content.[10] Figure 7 shows a plot of percent porosity versus stack (slice) position in which the slices go from the bottom (zero position) to the top of the block in the upward vertical direction as defined by the CT scan geometry. The peak of just over 1.5% porosity at a height of about 57 mm is the location of the combined maximum 2-D size of the two largest voids in block C4, which both have a volume of approximately 117 mm^3

(7.14×10^{-3} in^3). The next largest pore has a volume of 39.7 mm^3 (2.42×10^{-3} in^3) and the overall porosity of the entire block is only 0.39%. The porosity very near the top of the block peaks at about 1.8%, which is because of the presence of many similarly sized smaller pores as opposed to a few very large voids. This is illustrated in Fig. 8, which shows segmented binary images from the image (slice) stack of block C4 at the bottom (zero position), peak of about 0.6% porosity at a height of about 23 mm, peak at a height of about 57 mm, and the peak very near the top of the image stack from left to right.

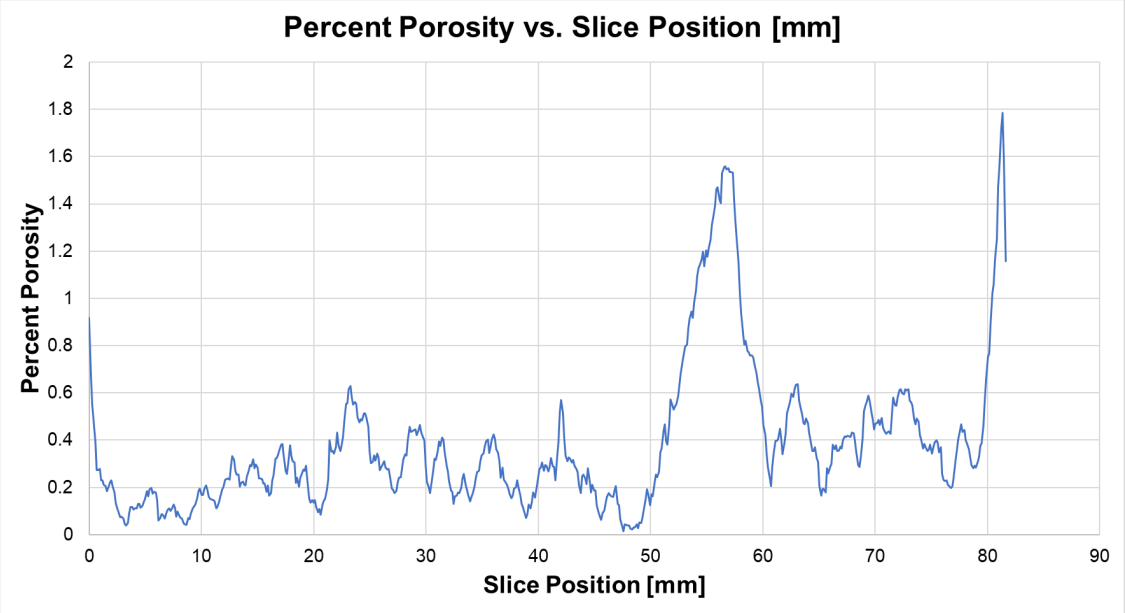

Fig. 7 Plot of percent porosity (%) vs. stack (slice) position (mm) in the slice image stack of block C4

Fig. 8 Segmented binary images from the image (slice) stack of block C4 at the bottom (zero position) (left), peak of about 0.6% porosity at height of about 23 mm, peak at height of about 57 mm, and peak very near the top of the image stack from left to right

Figure 9 shows the number of pores versus stack (slice) position in which the slices go from the bottom (zero position) to the top of the block in the upward vertical direction as defined by the CT scan geometry. It is evident that the number of pores varies locally from slice to slice up the stack, but overall it appears to fluctuate above and below a relatively flat or horizontal mean line except for very near the top. The number of pores versus slice position and percent porosity versus slice position plots have a different shape except for very near the top. In other words, the number of pores does not track with percent porosity as a function of slice position. This indicates that the size of the pores has a greater effect on the percent porosity than the overall number of pores.

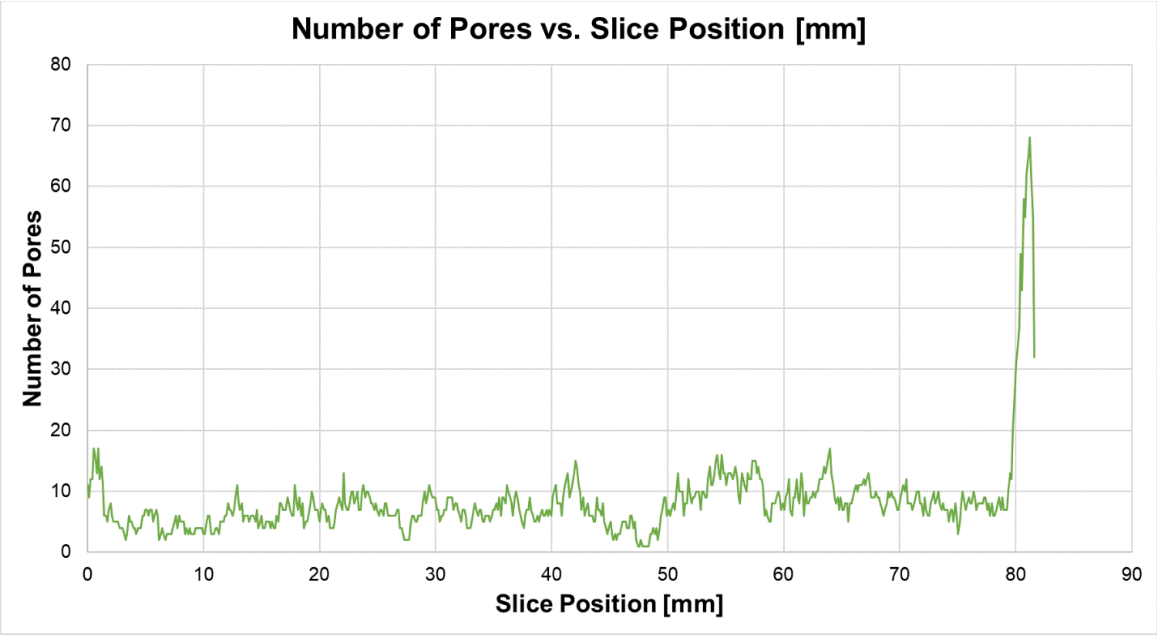

Fig. 9 Plot of number of pores vs. stack (slice) position (mm) in the slice image stack of block C4

Figure 10 shows the number of pores in pore volume bands starting at (0.0025 - <0.005) mm^3 and getting larger by 0.0025 mm^3 increments. This was based on a cubic voxel volume of (0.1314)(0.1314)(0.1314) mm^3 = 2.269×10^{-3} mm^3. The slight hump in about the middle of the pore volume bands with number of pores ranging from 16 to 25 has a pore volume range of (0.045 mm^3 – < 0.0625 mm^3). The smallest pores having volumes slightly larger than one cubic voxel are most numerous (818) with the number of pores dropping by almost an order of magnitude within the next higher volume band. The number of pores (48) has dropped by over an order of magnitude within the (0.0125 mm^3 – < 0.0150 mm^3) volume band and continues trending downward until the slight hump in the plot, after which it drops again much less steeply and then basically flattens out. This plot was done for relatively smaller pores beginning with

volumes slightly larger than one cubic voxel because the volume bands at the smaller end of the size spectrum are all populated. At the larger end of the volume spectrum, the bands are not all populated using the 0.0025 mm^3 increment with very large gaps among the largest pore volumes. For example, the volumes of the 10 largest pores are 21.39, 23.79, 24.70, 26.01, 26.59, 28.70, 37.76, 39.66, 117.1, and 117.2 mm^3. As previously stated, it is apparent how the nature of the porosity and void features change from near the outside of the block to the center of the block. This is likely due to the ingot slice cooling from the outside first to the inside last, producing more dendritic grain structure toward the outside as opposed to more equiaxed grain structure on the inside.[12]

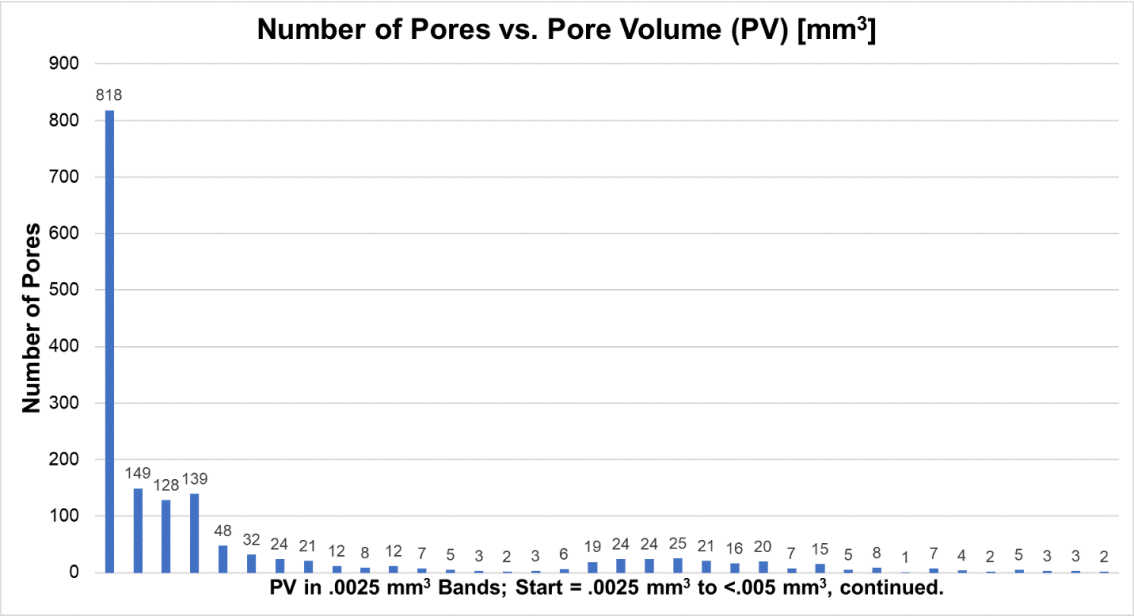

Fig. 10 Histogram plot of the number of pores vs. pore volume band (category) starting at (0.0025 – <0.005) mm^3 and increasing by 0.0025 mm^3 increments

Figure 11 shows top (a), front (b), and side (c) views of the 3-D volume of the block with porosity and voids in red and nominal material in light gray. The two individual largest roughly oval-shaped voids in the block are readily apparent in each image. Each image, especially in the top view, also exhibits the more linear and asymmetric nature of the porosity toward the outside and corners of the block. It is emphasized that these images are orthogonal views through the entirety of the block, so all the segmented porosity and voids are shown.

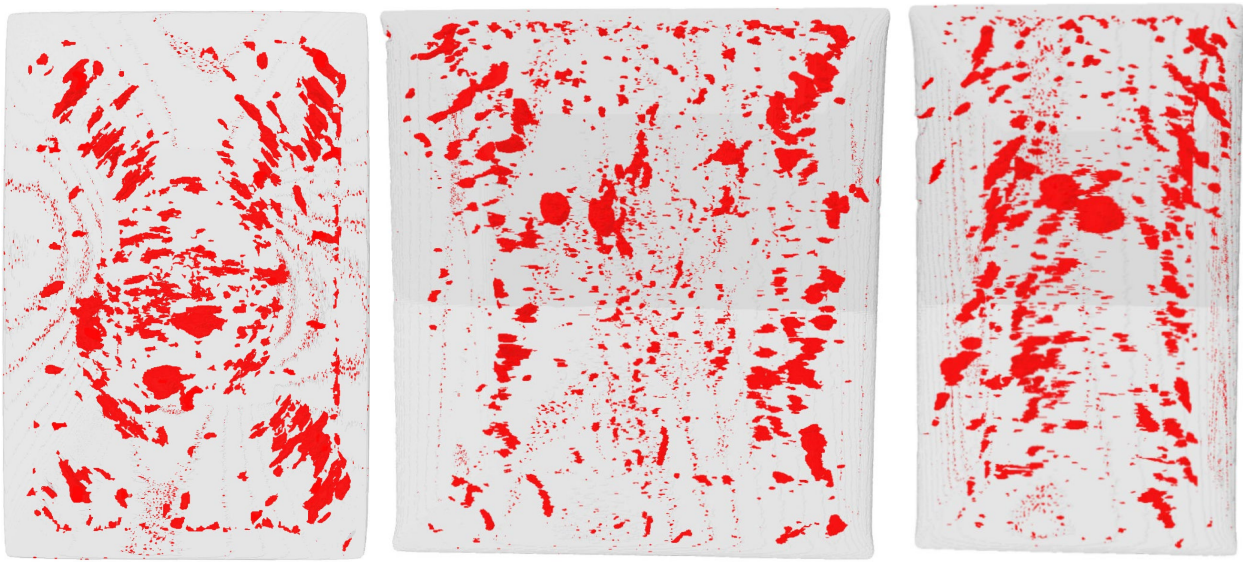

a. Three-dimensional top view b. Three-dimensional front view c. Three-dimensional side view

Fig. 11 Top (a), front (b), and side (c) 3-D views of the volume of block C4 with porosity and voids in red and nominal material in light gray

5. Summary and Conclusions

Several sectioned FeMnAl steel alloy blocks were XCT scanned using frame averaging and oversampling with a 450-kV conventional source in the 400-µm focal spot size mode. Results showed that the A and B blocks sectioned from the perimeter of the cast billet have overall better quality than the C blocks as determined by the number and sizes of detected discontinuities or features. The A blocks have the highest quality with block A3 having no discernible discontinuities and blocks A2 and A4 having small voids, except for the atypical larger void in A4. The B blocks contain a combination of small voids, short cracks, and missing material along edges or in corners. However, the A and B blocks do not have the extended and asymmetric crack-like features nearer to the outside of the blocks that all the C blocks have. The C blocks sectioned from the center of the cast billet contain higher levels of porosity with one or more relatively large voids near their centers and some voids intersecting edges or corners. The nature of the changes in the porosity and voids in the C blocks were likely due to the outside to inside cooling of the material.[12]

A series of advanced image processing techniques were applied to a set of cross-sectional axial slices (images) generated from the reconstructed volume of block C4 to isolate porosity and void features. Since the steel blocks were about 50.8 mm (2 inches) thick and about 76.2 × 76.2 mm (3 × 3 inches) in the orthogonal directions, they highly attenuated the X-ray flux during their CT scans, resulting in

low X-ray throughput and low-intensity X-ray image data at the detector. Mainly due to this and the resulting X-ray beam-hardening effects on the CT images, a simple global thresholding technique was not effective for segmenting porosity and voids from nominal steel material. NLM filtering and adaptive mean-based thresholding along with a number of other image processing techniques were used to systematically produce a consistent segmented binary representation of the porosity and voids in block C4. Two- and three-dimensional image analysis tools were then applied to the binary slice (image) stack to produce both volumetric quantitative porosity/void level data as well as complete 3-D visualizations of the porosity and voids alone within block C4.[10] The level of or percent porosity within block C4 from bottom to top (i.e., vertically through the image [slice] stack) is both relatively low and consistent, with maximum values located at the largest planar dimensions of the two biggest voids in the block and very near the top of the block. Even though the porosity and voids in block C4 appear to be extensive after isolating them and looking through the *entire* block, the porosity and void content of the entire block is only 0.39%. The number of pores within block C4 from bottom to top essentially fluctuates a small amount above and below a relatively flat or horizontal mean line and is not the same shape as the percent porosity versus stack (slice) position plot, which has clearly identifiable local maxima. This indicated that the sizes of the pores had a greater effect on the percent porosity than the overall number of pores. The smaller end of the pore volume distribution starting at a little above one cubic voxel (2.269×10^{-3} mm^3) was also plotted, which showed a relatively steep asymptotic drop-off from the smallest volume range (0.0025 – <0.005 mm^3) to larger volume ranges. The number of pores dropped by over an order of magnitude within the (0.0125 mm^3 – < 0.0150 mm^3) volume band and continued trending downward until a very slight hump in the plot, after which it dropped again much less steeply and then basically flattened out. As the porosity or voids become orders of magnitude larger, they become much less frequent on the same scale with large differences from one pore or void size to the next larger one (i.e., fractions of a millimeter or millimeters).

It is often the goal of image processing of XCT data to generate binarized or multilevel discrete image sets using straightforward global thresholding or simple variations thereof. Sometimes this is possible with very low or low noise, high signal, and high contrast data sets with sufficient gray scale separation between and definition of features. For example, this can be the case when analyzing XCT data of castings and forgings for porosity, voids, inclusions, cracks, tears, and other typical discontinuities in these materials. However, in cases of thick or highly attenuative (or both) materials in which beam hardening or artifacts (or both) will occur, as in this report, any number of more advanced processing methods may need to be used to generate representative binarized image sets for subsequent

quantitative analysis. The work described here utilized a subset of a significantly wider set of methods for image denoising and segmentation, material dilation and erosion, and other segmented image processing techniques. The methods collectively applied in this work are not limited to very high X-ray attenuation XCT data of FeMnAl steel alloys but could be used to process, segment, and analyze similar relatively low X-ray throughput, noisy, and low-contrast data sets with significant beam hardening or artifact (or both) content. In addition, the overall set of steps taken to maximize noise reduction while minimizing information (or signal) loss, application of flexible, adaptive thresholding for image segmentation, and multistep operations on binarized images to generate representative quantitative results is applicable to these types of nonideal data sets in general, as reasonable variations of this approach may be as well.

6. References

1. ASTM E 1570-95a. Standard practice for computed tomographic (CT) examination. Columbus (OH): American Society for Testing and Materials (ASTM); 1995.

2. Dennis MJ. Industrial computed tomography. In: Ahmad A, Bond LJ, editors. ASM handbook. Cleveland (OH): American Society for Metals (ASM) International; 1989. (Nondestructive evaluation and quality control; vol. 17).

3. Newton TH, Potts DG, editors. Radiology of the skull and brain. St. Louis (MO): The C.V. Mosby Company; 1981. (Technical aspects of computed tomography; vol. 5).

4. Stanley JH. Physical and mathematical basis of CT imaging. Columbus (OH): American Society for Testing and Materials (ASTM); 1986. ASTM CT Standardization Committee (E7.01.07), ASTM Tutorial: Section 3.

5. ASTM E 1441-95a. Standard guide for computed tomography (CT) imaging. Columbus (OH): American Society for Testing and Materials (ASTM); 1995.

6. Muehlhauser B. Optimizing image signal to noise ratio using frame averaging. North Star Imaging Blog; 2015 [accessed 2020 March 31]. https://4nsi.com/blog/2015/10/21/optimizing-image-signal-to-noise-ratio-using-frame-averaging/.

7. Shannon CE. Communication in the presence of noise. Proceedings of the Institute of Radio Engineers. 1949;37(1):10–21.

8. Buades A, Coll B, Morel JM. A non-local algorithm for image denoising. Proceedings of the 2005 IEEE Computer Society Conference on Computer Vision and Pattern Recognition (CVPR'05); 2005; San Diego, CA. pp. 60–65.

9. Buades A, Coll B, Morel JM. On image denoising methods. 123 seminars only; n.d [accessed 2020 March 31]. http://www.123seminarsonly.com/Seminar-Reports/029/42184313-10-1-1-100-81.pdf.

10. Bruker Corporation. Manual for Bruker-microCT CT-Analyser v. 1.13. Billerica (MA): Bruker Corporation; 2013.

11. Ferreira T, Rasband W. ImageJ user guide, IJ 1.46r. 2012 [accessed 2020 March 31]. https://imagej.nih.gov/ij/docs/guide/.

12. Richards V. MET 307 [course syllabus]. [Rolla (MS)]: Missouri S&T; 2013. Chapter 4, Risering of castings.

List of Symbols, Abbreviations, and Acronyms

2-D	two-dimensional
3-D	three-dimensional
ARL	Army Research Laboratory
CCDC	US Army Combat Capabilities Development Command
FeMnAl	iron-manganese-aluminum
fps	frame/s
NLM	nonlocal means
S/N	signal-to-noise
XCT	X-ray computed tomography

1 (PDF)	DEFENSE TECHNICAL INFORMATION CTR DTIC OCA
1 (PDF)	CCDC ARL FCDD RLD CL TECH LIB
8 (PDF)	CCDC ARL FCDD RLW MB W GREEN B CHEESEMAN D FIELD K LIMMER J SIETINS T WALTER J SUN C PERGANTIS